Symmetry and vibrationally resolved absorption spectra near the N *K* edges of N_2O: Experiment and theory

M. Ehara,[1,2,3,4,*] T. Horikawa,[3] R. Fukuda,[1,2,4] H. Nakatsuji,[4,5] T. Tanaka,[6] H. Kato,[6] M. Hoshino,[6] H. Tanaka,[6] R. Feifel,[7,8] and K. Ueda[8]

[1]*Institute for Molecular Science, 38 Nishigonaka, Myodaiji, Okazaki, 444-8585, Japan*
[2]*Research Center for Computational Science, Okazaki 444-8585, Japan*
[3]*Graduate University for Advanced Studies, Okazaki 444-8585, Japan*
[4]*JST, CREST, Sanboncho-5, Chiyoda-ku, Tokyo 102-0075, Japan*
[5]*Quantum Chemistry Research Institute, Goryo Oohara 1-36, Nishikyo-ku, Kyoto 615-8245, Japan*
[6]*Department of Physics, Sophia University, Tokyo 102-8554, Japan*
[7]*Department of Physics and Astronomy, Uppsala University, Box 516, SE-751 20 Uppsala, Sweden*
[8]*Institute of Multidisciplinary Research for Advanced Materials, Tohoku University, Sendai 980-8577, Japan*

(Received 13 December 2010; published 8 June 2011)

In this study, angle-resolved energetic-ion yield spectra were measured in the N 1*s* excitation region of N_2O. A Franck-Condon analysis based on *ab initio* two-dimensional potential energy surfaces of the core-excited Rydberg states, which were calculated by the symmetry-adapted cluster-configuration interaction method, reproduced observed vibrational excitations specific to the individual Rydberg states well and enabled quantitative assignments. Geometric changes in the terminal nitrogen N_t 1*s* and the central nitrogen N_c 1*s* excited states with respect to the $3p\pi$, $3p\sigma$, and $4s\sigma$ transitions were analyzed. The coupling of these valence and Rydbergs states was examined based on the second moment analysis. Irregular Rydberg-state behavior in the N_c $1s^{-1}$ $4s\sigma$ state was observed.

DOI: 10.1103/PhysRevA.83.062506 PACS number(s): 31.15.A−, 78.70.Dm, 33.20.−t, 06.30.Bp

I. INTRODUCTION

Inner-shell absorption spectroscopy [1,2], which is usually performed today at high-flux and high-resolution synchrotron radiation beamlines that are the successors to those of the original electron-energy-loss spectroscopy (EELS) technique [3], provides important information about the electronic structure and nuclear dynamics of core-excited species. Interpretation of the spectral features observed is often made by comparison with known spectra of related systems within the equivalent core model (ECM) [4], or, if available, based on theoretical calculations. In the case of randomly oriented free molecules, the drawback of traditional angle-integrated EELS and photoabsorption spectroscopy is that these techniques are insensitive to the symmetries of the excited electronic states and information from these states is often vital for making unambiguous assignments, in particular if several electronic states overlap or even coincide.

A breakthrough for gas phase soft x-ray absorption spectroscopy in this respect has been the introduction of angle-resolved yield measurements of fragment ions of inner-shell excited linear molecules [5–7]. Within the validity of the axial-recoil approximation [8,9], symmetry information can be extracted for linear molecules from this technique according to the following principle: For absorption transitions of $\Delta\Lambda = 0$ (i.e., $\Sigma \rightarrow \Sigma$, $\Pi \rightarrow \Pi$, etc.), fragment ions are preferentially detected parallel to the direction of the electric field vector of the linear polarized light, whereas for absorption transitions of $\Delta\Lambda = \pm 1$ (i.e., $\Sigma \rightarrow \Pi$, $\Pi \rightarrow \Sigma$, etc.), fragment ions are detected preferentially perpendicular to the direction of the electric field vector [10]. This method is therefore often referred to as "symmetry-resolved" x-ray absorption spectroscopy [10].

The N_2O molecule, with its two nonequivalent nitrogen atoms, the terminal N_t and the central N_c, has a linear geometry in the neutral ground state and the related electronic configuration can be denoted as [11]

$$(1\sigma)^2(2\sigma)^2(3\sigma)^2(4\sigma)^2(5\sigma)^2(6\sigma)^2(1\pi)^4(7\sigma)^2(2\pi)^4({}^1\Sigma^+),$$

where 1σ, 2σ, and 3σ correspond to the O 1*s*, N_c 1*s*, and N_t 1*s* core orbitals, respectively.

Several studies on core-excited N_2O have been reported previously. Promoting one of the core electrons into the lowest unoccupied molecular orbital π^* leads to the O $1s^{-1}$ π^*, N_c $1s^{-1}$ π^*, and N_t $1s^{-1}$ π^* Π states, respectively, as observed in the pioneering EELS studies of Wight and Brion [12] and Tronc *et al.* [13] in the 1970s. At about the same time, the first nitrogen *K*-shell photoabsorption spectrum of N_2O was recorded at Stanford [14], which agreed well with the EELS measurements and confirmed the assignments made based on the ECM. In the early 1990s Ma *et al.* [15] succeeded in recording a substantially improved, high-resolution photoabsorption spectrum of N_2O at the nitrogen *K* edges, which revealed many more electronic states than seen before and readily suggested that vibrational fine structures were present, but their assignments were only tentative.

Adachi *et al.* [16] presented the first high-resolution angle-resolved energetic-ion yield (ARIY) absorption spectra of the N 1*s* and O 1*s* excited states of N_2O, and investigated them with the help of *ab initio* self-consistent-field (SCF) calculations with explicit consideration of the core hole. They paid special attention to the O 1*s*, N_c 1*s*, and N_t 1*s* $\rightarrow$ π^* excitations and showed conclusively that Renner-Teller

*ehara@ims.ac.jp

coupling is present in all three excitations, which breaks the degeneracy of these states by bending the linear molecule. This is fundamental for an understanding of related coincidence experiments on N_2O performed at the corresponding photon energies [17–20]. As some studies have recently shown, the Renner-Teller effect in these three Π states is generally even more pronounced in a hot target gas [21] compared with N_2O molecules at room temperature. The work of Adachi *et al*. [16] further demonstrates that no Renner-Teller effect is present in any of the $1s \rightarrow$ Rydberg excited states, which suggests that the axial-recoil approximation is fully valid in these cases and allows reliable symmetry information from ARIY measurements in the corresponding spectral regions to be obtained. Based on the symmetry information available from their data, in combination with *ab initio* calculations and spectral features readily observed by Ma *et al*. [15], several new assignments were made by Adachi *et al*. [16].

Later, Prince *et al*. [22] recorded near-edge total-yield x-ray absorption fine-structure spectra without symmetry resolution, but with high statistics and unprecedented higher energy resolution at the N 1*s* and O 1*s* edges of N_2O. They obtained assignments of the spectral features via analysis of the quantum defects of the Rydberg states, the use of the ECM and by comparison to previously published photoabsorption and fragment ion spectra. In particular, several new Rydberg states converging to the oxygen *K* edge, including spectral features that could be assigned to certain vibrational modes, were revealed in their study.

Previously, we investigated the O 1*s* excited states of N_2O using ARIY spectroscopy [23,24]. Vibrationally resolved spectra were examined by Franck-Condon (FC) analysis based on *ab initio* calculations and revealed geometric changes in these states. The symmetry-adapted cluster-configuration interaction (SAC-CI) method [25,26] was used within the ECM approximation. The SAC-CI method has been established for investigating excited states of molecules in the fields of chemistry and physics, and in particular it has been successfully applied to various types of core-electronic processes [27–29]. Noticeably, in our previous work [23], the irregular behavior in the $\Sigma-$symmetry spectrum of O 1*s* excited states of N_2O was interpreted by coupling of the valence and Rydberg states using the electronic part of the second moments. The thermal effect on the coupling of the valence and Rydberg states in the O 1*s* excited states of N_2O was also studied [24].

In this work we examine state-of-the-art symmetry-resolved soft x-ray absorption spectra of N_2O measured with high-photon energy resolution in the vicinity of the two N *K* edges and analyze them with accurate SAC-CI calculations. Having symmetry resolution and high-photon energy resolution at hand enables us to disentangle spectral features observed previously in high-resolution angle-integrated measurements, and to reveal new spectral lines, some of which can be attributed to regular vibrational progressions of previously identified Rydberg states and some of which are proposed to belong to hitherto unobserved Rydberg states. FC analysis based on *ab initio* two-dimensional (2D) potential energy surfaces (PESs) explains the detailed vibrational structure and geometry changes in these spectra.

II. EXPERIMENT

The experiments were performed at the c branch of the photochemistry beamline 27SU at SPring-8, Japan, which was equipped with a high-resolution soft x-ray monochromator with a varied-line-space grating [30,31]. The radiation source was a figure-8 undulator, which provided horizontally or vertically linear polarized light after the undulator gap was set appropriately [32,33]. Two ion detectors, each of which had a retarding potential of 6 V for detecting ions with kinetic energies higher than 6 eV, were mounted at 0° and 90° with respect to the electric field vector **E** of the synchrotron light [34]. The ion detectors were used for recording the symmetry-resolved near-edge x-ray absorption fine-structure spectra. The acceptance angle for fragment ions in the detectors was $\sim\pm 9°$. The ratio of the detection efficiencies of the two detectors was determined by comparing the ARIY spectra recorded using horizontal and vertical linear polarized light. The ratio was close to unity after careful alignments of the two detectors and careful settings of the high voltages on the two detectors. A 4π-sr time-of-flight (TOF) ion detector was placed 250 mm away from the other two detectors and was used to record the total ion yield (TIY) simultaneously with the ARIYs. The photon energy bandwidth of the monochromator was set at 50 meV. The monitor of the photon flux for normalization was made by a drain current after the gas sample. All spectra were normalized to the data acquisition time, gas pressure, and photon flux. The photon energy scale was calibrated using the EELS spectra of Wight *et al.* [12] as a reference. N_2O gas was commercially obtained with a stated purity $<99.99\%$.

III. COMPUTATIONAL DETAILS

Two-dimensional PESs of the ground and the N 1*s* core-excited states were calculated along the direction of the normal coordinates q_1 and q_3 corresponding to the quasi-symmetric (ν_1') and quasi-antisymmetric (ν_3') stretching vibrational motions, respectively, in the ranges $R_{\rm NN} = 1.00-1.30$ Å and $R_{\rm NO} = 1.00-1.55$ Å. The basis sets were correlation-consistent polarized valence triple-ζ (cc-pVTZ) basis sets without f function, as proposed by Dunning, namely [4*s*3*p*2*d*] [35], plus Rydberg functions [5*s*5*p*] [36] placed on the N_c atom for describing $n = 3$, 4, 5 (*s* and *p*).

The ground- and core-excited states of N_2O were calculated by the SAC and SAC-CI methods, respectively. Ground-state geometry was obtained as $R_{\rm NN} = 1.122$ and $R_{\rm NO} = 1.184$ Å by the SAC method, in good agreement with the experimental values of 1.127 and 1.185 Å [23,37], respectively. The N 1*s* core-excited states were calculated by two approaches of the SAC-CI SD-*R* method in which single (S) and double (D) excitations were adopted for the *R* operators. One approach calculated the core-excited states directly (without ECM) and the other adopted the ECM approximation. Both approaches have advantages and disadvantages. The SAC-CI method, which calculates the core-excited states directly, describes the orbital relaxation of the core-electron process as it is and solves the N_t 1*s* and N_c 1*s* excited states simultaneously while including the interactions between them. The core-excited states, however, usually have large orbital relaxation for

which higher excitation operators are required to give an accurate description. Therefore, the SAC-CI SD-*R* calculation is sometimes not sufficient to calculate core-excited states. In such a case, the inclusion of higher excitation operators in the expansion, the SAC-CI general-*R* method, is necessary; however, we note that the general-*R* method is computationally expensive in the present implementation. The SAC-CI method using the ECM approximation, in contrast, calculates the N_t 1*s* and N_c 1*s* excited states separately. It is usually stable even for the higher Rydberg states and is computationally cost effective, although it describes the orbital relaxation of the core-electronic processes by the ECM approximation. To this end, we conducted both types of SAC-CI calculations and interpreted the results by comparing them with the experimental spectra. In what follows, we denote the latter method as SAC-CI ECM.

In comparing the SAC-CI and SAC-CI ECM results, the PESs were similar to each other except for the N_t $1s^{-1}$ $3s\sigma$ state as discussed later. Therefore, to calculate the 2D PESs of the core-excited states and theoretical vibrational spectra, we used the SAC-CI ECM method which is stable and cost effective. For the N_t 1*s* and N_c 1*s* core-excited states, the excited states of ONO and NOO, respectively, were calculated by the SAC-CI ECM method [25,26]. The excited states of the neutral radicals, ONO and NOO, were calculated by an electron attachment scheme of SAC-CI applied to the closed-shell ONO^+ and NOO^+ ions, respectively. In the SAC-CI SD-*R* calculations, we used an algorithm that calculates σ vectors directly and includes all the S_2R_1 and S_2R_2 nonlinear terms [38], namely the direct SAC-CI method. All the *S* and *R* operators were included without perturbation selection in the SAC-CI calculations. We also adopted the nonvariational method for solving the SAC-CI equations. The equilibrium geometries of each state were obtained from the analytic energy gradients of the SAC-CI method. The optimized structures were also confirmed to be local minima by calculating the PESs in the bending coordinate.

The vibrational analysis was performed using the SAC-CI ECM 2D PESs of the N_t 1*s* and N_c 1*s* excited states of N_2O. To calculate the FC factors of the vibrational spectrum, the vibrational wave function was obtained by the grid method, in which the Lanczos algorithm was adopted for the diagonalization. The 2D PESs of the N_2O molecule were described in the binding coordinates where the bond distances were r_1 and r_2, and the bond angle was fixed at 180°. In this coordinate, the kinetic energy (*T*) part of the Hamiltonian of the vibrational motion was given by:

$$T = \frac{p_1^2}{2\mu_{N_cN_t}} + \frac{p_2^2}{2\mu_{N_cO}} + \frac{p_1 p_2}{m_{N_c}}, \quad p_k = -i\frac{\partial}{\partial r_k}, \quad k = 1,2, \tag{1}$$

where $\mu_{N_cN_t}$ (μ_{N_cO}) is the reduced mass of the N_t and N_c (N_c and O) atoms. The coordinates r_1 and r_2 were represented by the Hermite discrete variable representation (DVR). The 2D PESs were fitted to the analytic functions of the fifth-order 2D Morse expansion:

$$V(r_1,r_2) = \sum_{i,j=0}^{5} B_{ij}(1 - e^{-a_1(r_1-r_{e_1})})^i(1 - e^{-a_2(r_2-r_{e_2})})^j, \tag{2}$$

where r_{e_1} and r_{e_2} are equilibrium distances and are determined by the analytic energy gradients of the SAC method or the SAC method with CI, B_{ij} are expansion coefficients of the PESs, and a_1 and a_2 denote the parameters in the 2D Morse function. The vibrational spectra were calculated in the framework of the FC approximation.

SAC-CI calculations were performed with the GAUSSIAN 09 suite of programs [39] with some changes for calculating core-excited states. For calculating the vibrational states and FC factors, the multiconfiguration time-dependent Hartree (MCTDH) program package [40] was used.

IV. RESULTS AND DISCUSSION

A. N_t 1*s* excitation

Figure 1 shows a high-resolution TIY photoabsorption spectrum (upper panel) of N_2O in the 399–407-eV photon energy region, together with the corresponding ARIY spectra measured at angles of 0° (middle panel) and 90° (lower panel), respectively. The assignments were mainly based on the present calculations and partially based on previous works, in particular the *ab initio* calculations of Adachi *et al.* [16] and the ECM-based study of Prince *et al.* [22], as well as on the analysis of the quantum defects for the various series. They are summarized in Table I where the assignments of Adachi *et al.* [16] and Prince *et al.* [22] are also included for comparison.

Figure 2 represents the 405.5–408.5-eV photon energy region of the high-resolution TIY photoabsorption spectrum (upper panel) of N_2O together with the corresponding ARIY

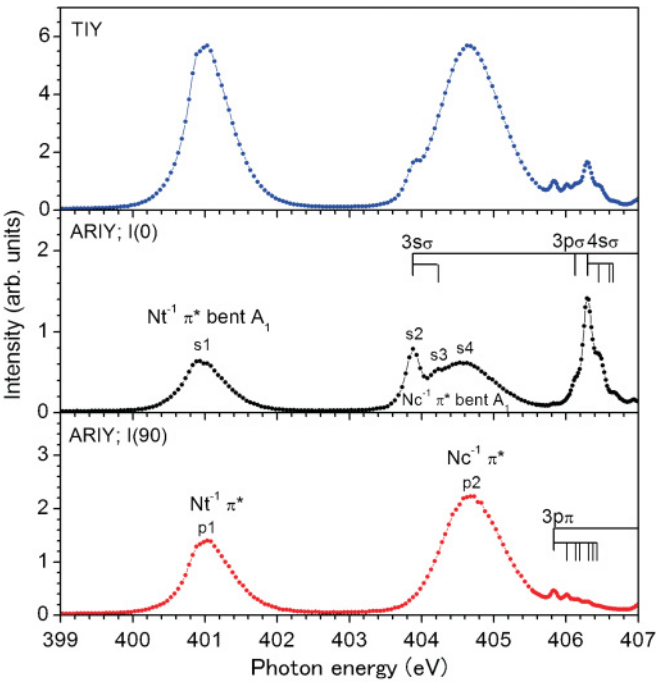

FIG. 1. (Color online) High-resolution nitrogen *K*-edge total ion yield (TIY) and angle-resolved ion yield (ARIY) spectra of N_2O recorded in the photon energy range between 399 and 407 eV. Upper panel: TIY spectrum; middle panel: ARIY spectrum of the Σ channels ($\Delta\Lambda = 0$); lower panel: ARIY spectrum of the Π channels ($\Delta\Lambda = 1$).

TABLE I. Energies, assignments and quantum defect δ for the N 1*s* Rydberg states identified in the ARIY spectrum of Figs. 1 and 2.

Peak	Expt.(eV)	Theory (eV)	Assignment	δ	Prince	Adachi
s1	400.95		3π bent A_1 (N_t)			
p1	401.03		3π linear B_1 (N_t)		3π (N_t)	3π (N_t)
s2	403.88		$3s\sigma$ (N_t)	1.27	$3s\sigma$ (N_t)	$3s\sigma$ (N_t)
s3	404.23		$3s\sigma$ (N_t) (001)			
s4	404.58		3π bent A_1 (N_c)			
p2	404.68		3π linear B_1 (N_c)		$3s\sigma$ (N_c)	$3s\sigma$ (N_c)
p3	405.83	405.83[a]	$3p\pi$ (N_t)	0.72	$3p\pi$ (N_t)	$3p\pi$ (N_t)
p4	406.01	406.01	$3p\pi$ (N_t) (100)		$3p\pi$ (N_t) (001)	$3p\pi$ (N_t) + ν
s5	406.13	406.07[b]	$3p\sigma$ (N_t)	0.57		
p5	406.13	406.12	$3p\pi$ (N_t) (001)		$3p\pi$ (N_t) (101)	
p6	406.17	406.19	$3p\pi$ (N_t) (200)		$3p\pi$ (N_t) (101)	
s6	406.29	406.29[c]	$4s\sigma$ (N_t)	1.48	$4s\sigma$ (N_t)	$4s\sigma$ (N_t)
p7	406.30	406.30	$3p\pi$ (N_t) (101)			
s7	406.45	406.46	$4s\sigma$ (N_t) (100)		$4s\sigma$ (N_t) (001)	
p8	406.45	406.37	$3p\pi$ (N_t) (002)			
		406.41	$3p\pi$ (N_t) (300)			
s8	406.67	406.62	$4s\sigma$ (N_t) (200)		$4s\sigma$ (N_t) (201)	
		406.65	$4s\sigma$ (N_t) (001)			
s9	406.93		$3d\sigma$ (N_t)	0.00		
p9	406.99		$3d\pi$ (N_t)	–0.06	$3d\pi$ (N_t)	$3d\pi$ (N_t)
s10	407.10		$3d\sigma$ (N_t) (100)			
p10	407.17		$3d\pi$ (N_t) (100)		$4p\pi$ (N_t)	
p11	407.25		$4p\pi$ (N_t)	0.62	$4p\pi$ (N_t)	$4p\pi$ (N_t)
s11	407.29		$4p\sigma$ (N_t)	0.55	$3d\sigma$ (N_t)	$3d\sigma$ (N_t)
s12	407.41		$5s\sigma$ (N_t)	1.37	$5s\sigma$ (N_t) (001)	
p12	407.43		$4p\pi$ (N_t) (100)			
s13	407.54		$3s\sigma$ (N_c) or $5s\sigma$ (N_t) (100)	1.34	$3s\sigma$ (N_c)	
s14	407.67		$3s\sigma$ (N_c) (100)		?	
s15	407.84		$6s\sigma$ (N_t)	1.24	$5p\pi$ (N_t)	$4p\sigma$ (N_t) or $3s\sigma$ (N_c)
s16	407.97		$6s\sigma$ (N_t) (100)		$6p\pi$ (N_t)	
p13	407.97		$6p\pi$ (N_t)	0.60	$6p\pi$ (N_t)	
s17	408.03		$7s\sigma$ (N_t)	1.24	$6p\pi$ (N_t)	
p14	408.17		$7p\pi$ (N_t)	0.60	$7p\pi$ (N_t)	$5p\pi$ (N_t)
s18	408.19		$8s\sigma$ (N_t)	1.24	$7p\pi$ (N_t)	
p15	408.33		$7p\pi$ (N_t) (100)		$8p\pi$ (N_t)	
s19	408.35		$8s\sigma$ (N_t) (100)		$8p\pi$ (N_t)	

[a]The calculated (000) level of the N_t $1s^{-1}$ $3p\pi$ state is set to 405.83 eV.
[b]The position of the (000) level of the N_t $1s^{-1}$ $3p\sigma$ state is calculated relative to the N_t $1s^{-1}$ $3p\pi$ state.
[c]The calculated (000) level of the N_t $1s^{-1}$ $4s\sigma$ state is set to 406.29 eV.

spectra measured at angles of 0° (middle panel) and 90° (lower panel), respectively. The N_t 1*s* ionization threshold, located at 408.43 eV, in accordance with the work of Alagia *et al.* [41], is included as a reference mark for assignment of the spectral features observed.

Figure 3 displays the PESs of the N 1*s* excited states of Σ and Π symmetries, which were obtained by the SAC-CI method calculating the core-excited states directly, where a one-dimensional cut was made at $R_{NN} = 1.10$ Å. The 2D PESs were calculated with the equal grid of 0.1 Å for R_{NN} and the cut was selected as it is close to the equilibrium N–N bond length. In this figure, the PESs of the N_t 1*s* and N_c 1*s* ionized states are also shown for reference. We also present the corresponding PESs of the N_t 1*s* excited states obtained by the SAC-CI ECM method shown in Fig. 4. The equilibrium geometries of the ground and low-lying N 1*s* excited states calculated from the analytic energy gradients of the SAC-CI method are summarized in Table II, which gives a comparison of the results for the SAC-CI and SAC-CI ECM calculations. In the SAC-CI calculations (without ECM), we also obtained the σ^* states regarded as shape resonances and nonphysical discrete continuum states with the character of the N_t (N_c) 1*s* excitation above the N_t (N_c) 1*s* ionization threshold. These are not included in Fig. 3. Furthermore, we present in Table III the oscillator strength obtained by the SAC-CI method calculating the core-excited states directly.

First, we discuss the PESs obtained by the SAC-CI and SAC-CI ECM calculations. As seen in the comparisons in Figs. 3 and 4, the nature of the PESs of N_t 1*s* excited states calculated by the two methods is similar except for the N_t $1s^{-1}$ $3s\sigma$ state. In the SAC-CI PESs of N 1*s* excited states shown by the diabatic representation (Fig. 3), some N_t and N_c

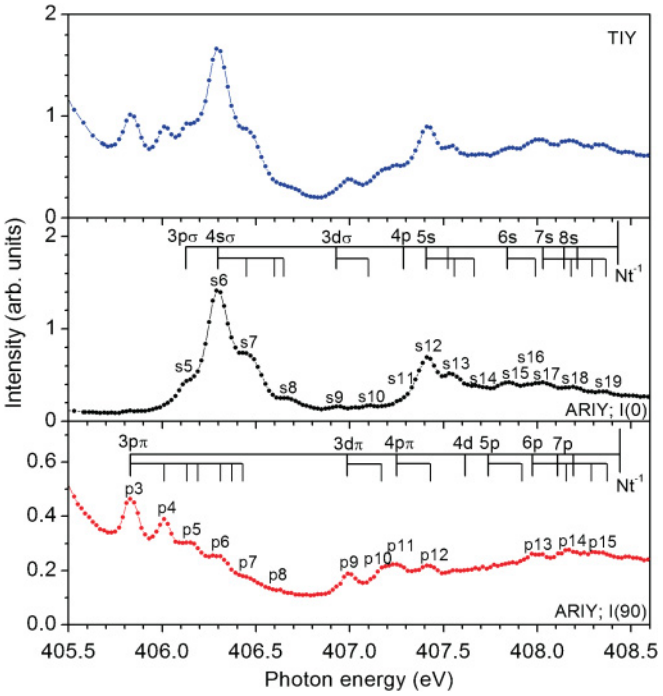

FIG. 2. (Color online) High-resolution nitrogen *K*-edge total ion yield (TIY) and angle-resolved ion yield (ARIY) spectra of N_2O recorded in the photon energy range between 405.5 and 408.5 eV. Upper panel: TIY spectrum; middle panel: ARIY spectrum of the Σ channels ($\Delta\Lambda = 0$); lower panel: ARIY spectrum of the Π channels ($\Delta\Lambda = 1$).

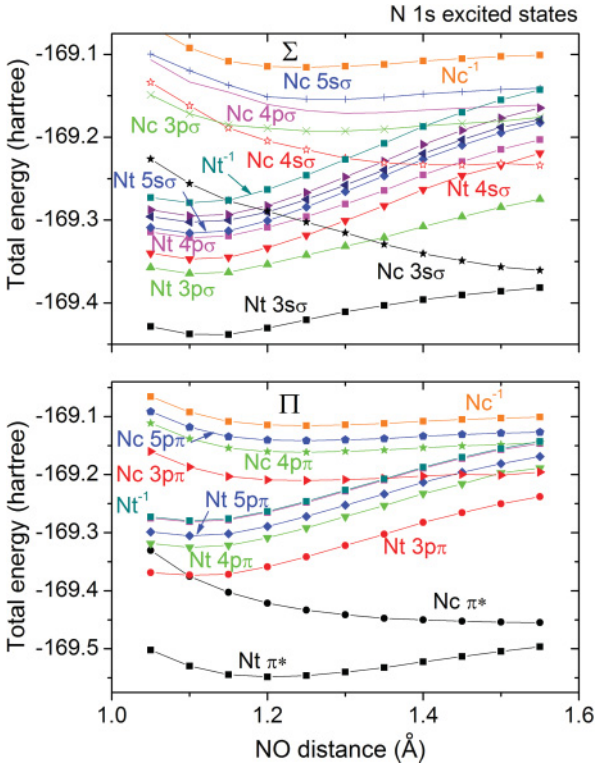

FIG. 3. (Color online) Potential energy curves of the N 1*s* excited states of N_2O for Σ and Π symmetry with the cut at $R_{NN} = 1.10$ Å. Calculations were carried out using the SAC-CI method (without ECM).

excited states cross each other because the N_c $1s^{-1}$ $3s\sigma$ and N_c $1s^{-1}$ $4s\sigma$ states have a repulsive character whose picture cannot be obtained by the SAC-CI ECM method. It should be noted that, at the crossing points, configuration interaction occurs and the N_t 1*s* and N_c 1*s* intermediate core-excited states exist at the potential seam. The PESs of the N_c excited states calculated by the two methods are also similar, as shown later. In addition to these calculations, we performed a geometry optimization of low-lying N_t 1*s* and N_c 1*s* excited states. The optimized structures are again similar between the SAC-CI and SAC-CI ECM calculations. For example, in the N_t $1s^{-1}$ $3p\sigma$ state, the optimized bond distances, $r_{NN} = 1.109$ Å and $r_{NO} = 1.102$ Å, calculated by SAC-CI, are similar to those calculated by SAC-CI ECM, $r_{NN} = r_{NO} = 1.120$ Å, whereas some are different, such as in the N_t $1s^{-1}$ $3s\sigma$, where the difference in the optimized r_{NN} distance is ∼0.43 Å between SAC-CI and SAC-CI ECM calculations. Because the full PES calculations by the SAC-CI SD-*R* method are difficult for some states, in particular the N_c excited states, and the truncation up to double excitation operators might not be sufficient for accurate description, we decided to analyze the experimental spectra mainly by the SAC-CI ECM calculations.

TABLE II. Equilibrium bond lengths of the N 1*s* excited states of N_2O optimized by the SAC-CI and SAC-CI ECM methods.

	SAC-CI ECM		SAC-CI	
State	R_{NN} (Å)	R_{NO} (Å)	R_{NN} (Å)	R_{NO} (Å)
N_t 1*s*				
$3s\sigma$	1.554	1.138	1.113	1.109
$3p\sigma$	1.120	1.120	1.109	1.102
$4s\sigma$	1.163	1.163	1.104	1.103
$3p\pi$	1.117	1.117	1.112	1.107
N_c 1*s*				
$3p\sigma$	1.127	1.243	1.104	1.280
$4s\sigma$	1.112	1.314	–	–
$3p\pi$	1.119	1.243	1.111	1.237

Two broad features centered around 400.98 eV and 404.6 eV photon energy (cf. Fig. 1) in the TIY spectrum are the well-known N_t $1s^{-1}$ π^* and N_c $1s^{-1}$ π^* resonances, respectively [10,12–16,21,22]. They are also present in the 0° measurements where their maxima are shifted by ∼0.1 eV towards lower photon energy because of the Renner-Teller effect, as discussed in detail previously [10,16]. Note that the PES of the N_t $1s^{-1}$ π^* state is bound in the N–O coordinate as in the O $1s^{-1}$ π^* excited states [23], whereas that of the N_c $1s^{-1}$ π^* state is repulsive in this coordinate as discussed further later in this paper. The oscillator strength of the N_t $1s^{-1}$ π^* transition was $f = 0.050$, which was smaller than the corresponding value for the N_c $1s^{-1}$ π^* transition, $f = 0.062$, which is in good agreement with the experimental spectra.

The comparatively sharp line located at 403.88 eV (s2) in the ARIY [I(0°)] spectrum (cf. Fig. 1), which is also discernible in the TIY spectrum as a shoulder (see also Ref. [22]) but which is completely absent in the ARIY [I(90°)] spectrum, has been identified previously as the N_t $1s \rightarrow 3s\sigma$ Rydberg state [10]. An additional spectral feature is readily visible

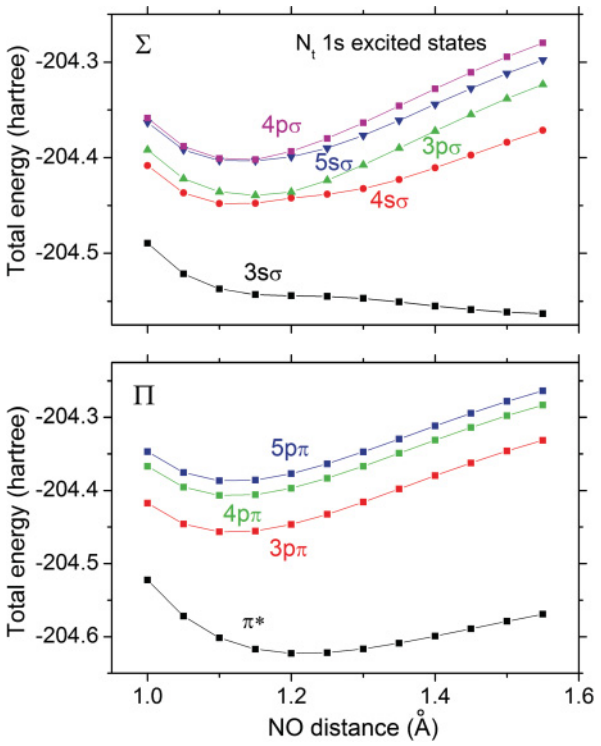

FIG. 4. (Color online) Potential energy curves of the low-lying N_t 1*s* excited states of N_2O for Σ and Π symmetry with the cut at $R_{NN} = 1.10$ Å. Calculations were carried out using the SAC-CI ECM method.

at ∼404.23 eV, which might be due to the ν_3 excitation of the $3s\sigma$ (N_t $1s^{-1}$) Rydberg state. Such an excitation may not be totally unexpected because the mixing of the Rydberg and valence states, as discussed previously [10], may result in distortion of the PES along the q_1 and/or q_3 normal coordinates. Furthermore, we also noticed that the peak width of the $3s\sigma$ excitation appeared to be broader than the $ns\sigma$ (N_t) peaks, which might further support this interpretation. The SAC-CI results in Fig. 3 show that the PES of the N_t $1s^{-1}$ $3s\sigma$ state is bound; however, the SAC-CI ECM results in Fig. 4 suggest that the PES of this state is quasibound and distorted. A possible explanation for this finding is that the repulsive character of this PES is overestimated in the SAC-CI ECM calculations. The difference between the calculated equilibrium bond distances is large between these methods; $R_{NN} = 1.113$ Å and $R_{NO} = 1.109$ Å by SAC-CI and $R_{NN} = 1.554$ Å and $R_{NO} = 1.138$ Å by SAC-CI ECM. According to the SAC-CI results, the additional broad band observed in the higher energy region of the vibrational structure may be attributed to the component of the π^* transition. The SAC-CI ECM calculations, in contrast, suggest the possibility of the transition occurring within the flat FC region of the PES of this state. The oscillator strength of this transition was calculated to be $f = 0.0042$, which is one order of magnitude smaller than that of the π^* transition.

The spectral region above 405.6-eV photon energy is quite complex because of the presence of several states of Σ and Π symmetry, which partially overlap or even coincide in the TIY recording, as seen from the angle-resolved measurements (middle and lower panels of Fig. 2). In particular, the line p3 at 405.83 eV, which is well resolved in the TIY and the ARIY [I(90°)] recordings, reflects the fundamental (000) vibrational line of the N_t $1s \rightarrow 3p\pi$ Rydberg state, as identified in previous studies [16,22]. The neighboring line (p4) at 406.01-eV photon energy, also well resolved in the TIY and the ARIY [I(90°)] spectra, has been proposed to be a further vibrational component of the N_t $1s^{-1}$ $3p\pi$ Rydberg state [16], and was recently assigned as the N_t $1s^{-1}$ $3p\pi$ (001) line [22]. The vibrational assignment for N_t $1s^{-1}$ excitations made by Prince *et al.* [22] was generally guided by the vibrational energy spacing from valence band photoemission data of the ECM molecule NO_2 [42]. We would rather use the frequency values of the N_2O neutral ground state as a guide for the vibrational assignment. According to a previous study [43], the ground-state vibrational spacing of the symmetric stretching mode (ν_1, primarily N–O stretch), the bending mode (ν_2), and the asymmetric stretching mode (ν_3, primarily N≡N stretch) is 159.3 meV, 73.0 meV, and 275.7 meV, respectively. Regarding the energy difference of 180 meV of the two lines under consideration, which is closest to the ν_1 value, we assigned the spectral line at 405.96 eV to the (100) component of the N_t $1s^{-1}$ $3p\pi$ Rydberg state. This assignment is also supported by the present calculations as discussed below. Additional lines towards the higher photon energy side of the (100) line are nicely revealed in the present ARIY [I(90°)] spectrum with about the same spacing and an intensity distribution typical for a vibrational band. They are assigned accordingly as higher vibrational components of the ($\nu_1$00) mode (cf. Table I). Clearly, the experimental data also give room to infer the ν_3 mode to be excited, as indicated in the lower panel of Fig. 2 and summarized in Table I.

For the N_t $1s^{-1}$ $3p\pi$ Rydberg state, the SAC-CI ECM calculations result in a large geometry change of the R_{NO} distance, and the calculated equilibrium bond distances of this state are $R_{NN} = R_{NO} = 1.117$ Å. A direct comparison between the SAC-CI ECM spectrum of the N_t $1s^{-1}$ $3p\pi$ state and the ARIY [I(90°)] spectrum is made in Fig. 5; the (000) vibrational level of the theoretical spectrum is set to the experimental level because the absolute excitation energy is not obtained in the ECM approximation. As can be seen, the theoretical spectrum reproduces the ARIY spectrum well and the vibrational structure is predominantly attributed to the ν_1 progression; in particular, the p3, p4, and p6 peaks are assigned to transitions to ($\nu_1$00) levels, and p5 and p7 to the (001) and (101) levels, respectively. The calculated vibrational spacings of the ν_1 and ν_3 modes were ∼180 and ∼290 meV, respectively, which are well in accordance with the experimental values of ∼180 and ∼300 meV, respectively. The oscillator strength of this transition is calculated to be $f = 0.0028$, which is reasonable compared with other transitions.

Returning to the TIY spectrum, a high intense band centered around 406.29 eV (s6) occurs in the photon energy region between ∼406 and ∼406.8 eV, which gets substantial contributions from states of Σ symmetry, as seen from the ARIY [I(0°)] recording. To date, the shoulder at 406.13 eV has been attributed to the (101) vibrational line of the N_t $1s^{-1}$ $3p\pi$ Rydberg state [22]. Although the $3p\pi$ state, in the form of a higher vibrational component [based on our assignment, the (001) and (200) lines], contributes to the intensity of this shoulder in the TIY spectrum, some nonnegligible intensity

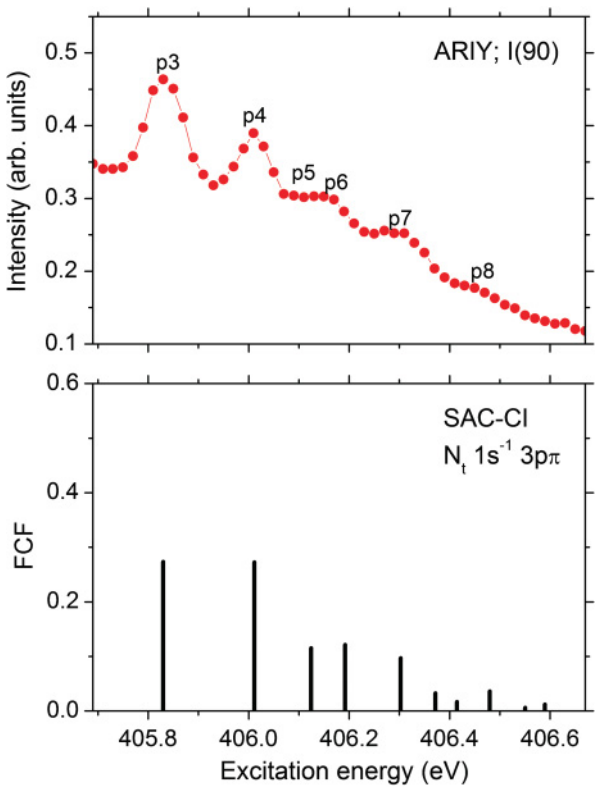

FIG. 5. (Color online) The ARIY [I(90°)] and SAC-CI ECM spectra of the N_t $1s^{-1}$ $3p\pi$ states of N_2O.

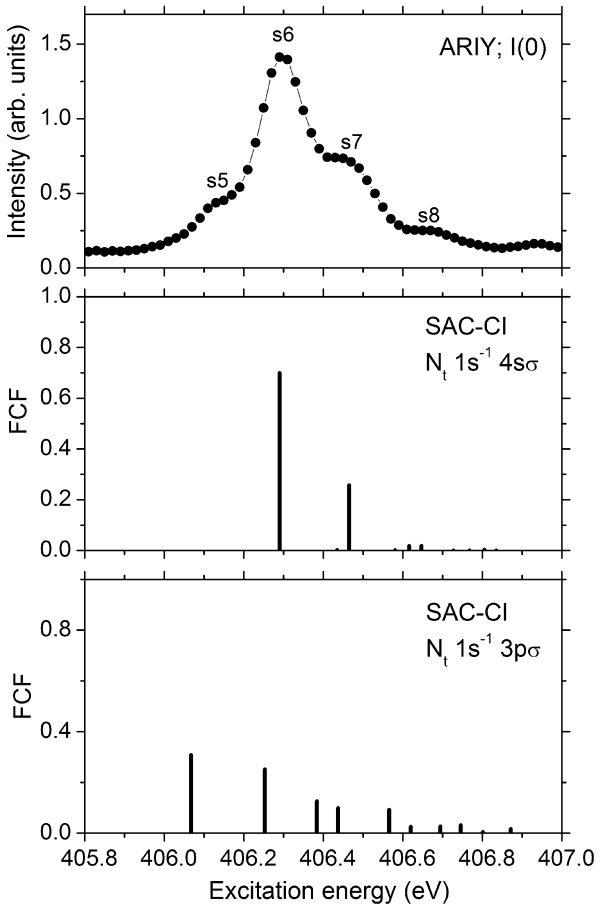

FIG. 6. The ARIY [I(0°)] and SAC-CI ECM spectra of the N_t $1s^{-1}$ $4s\sigma$ and N_t $1s^{-1}$ $3p\sigma$ states of N_2O.

also arises from a state of Σ symmetry. Regarding the most intense line located at 406.29 eV, which is the N_t $1s^{-1}$ $4s\sigma$ Rydberg state [16,22], and the two adjacent shoulders on the higher photon energy side, which have recently been attributed to vibrational excitations of the same state [22], we performed a least-squares curve-fitting analysis on this band of the ARIY [I(0°)] spectrum. The results of this analysis strongly support the interpretation that the most intense line at 406.29 eV photon energy and the two shoulders (s7, s8) on the higher photon energy side most likely represent the vibrational progression of the $(\nu_1 00)$ mode of the N_t $1s^{-1}$ $4s\sigma$ Rydberg state. Again, the experimental data allow for inferring the ν_3 mode to be excited, as indicated in the middle panel of Fig. 2. The shoulder at 406.13 eV (s5), however, is more likely to belong to a separate electronic state. A suitable candidate for the latter with respect to the quantum defect is the N_t $1s^{-1}$ $3p\sigma$ Rydberg state, which is also in accordance with the calculated oscillator strengths of Adachi *et al.* [16]. It is worth noting in this context that the unusually high intensity of the N_t $1s^{-1}$ $4s\sigma$ Rydberg state, in particular, has been rationalized [16] in terms of an underlying mixing of the valence and Rydberg states akin to the prominent O_2 case (e.g., [10] and references therein).

Theoretical vibrational spectra of the N_t $1s^{-1}$ $4s\sigma$ and N_t $1s^{-1}$ $3p\sigma$ states are presented in Fig. 6, together with the ARIY [I(0°)] spectrum. The excitation energy of the N_t $1s^{-1}$ $3p\sigma$ state is calculated relative to the N_t $1s^{-1}$ $3p\pi$ state including the zero-point energy correction within the ECM approximation, whereas the (000) peak of the N_t $1s^{-1}$ $4s\sigma$ state is fitted to the experimental one. In the present vibrational analysis, the diabatic picture was adopted for simplicity, although vibronic coupling between these states may exist. The geometry change of the N_t $1s^{-1}$ $4s\sigma$ state is relatively small compared with that of the O $1s^{-1}$ $4s\sigma$ [23] and the N_c $1s^{-1}$ $4s\sigma$; the calculated equilibrium bond distances of the N_t $1s^{-1}$ $4s\sigma$ state were $R_{NN} = R_{NO} = 1.163$ Å. Therefore, the spectrum shows a normal Rydberg-type structure and the s6 and s7 peaks are assigned to the $(\nu_1 00)$ levels, as seen in Fig. 6. The equilibrium geometry of the N_t $1s^{-1}$ $3p\sigma$ state, in contrast, is similar to that of the N_t $1s^{-1}$ $3p\pi$ state, and, therefore, the higher vibrational levels are also excited as in the N_t $1s^{-1}$ $3p\pi$ state. Note that the geometry optimization of the $4s\sigma$ and $3p\sigma$ states was performed in a different symmetry of D_{2h} as the Σ_g and Σ_u states, respectively. The s5 peak is attributed to the transition to the N_t $1s^{-1}$ $3p\sigma$ state, which was 0.15 eV lower than the N_t $1s^{-1}$ $4s\sigma$ state, whose energy separation is comparable to the experimental value of 0.16 eV. The transitions to higher vibrational levels of $(\nu_1 0 \nu_3)$ in the N_t $1s^{-1}$ $3p\sigma$ state are completely overlapped with the vibrational levels of the N_t $1s^{-1}$ $4s\sigma$ state, as seen in Fig. 6. The calculated oscillator strengths of the $4s\sigma$ and $3p\sigma$ transitions at the ground-state geometry are not as consistent with the experimental absorption intensity, even when the FC factors are considered; however, the oscillator strengths of these transitions depend on the geometry.

For evaluating the coupling of the valence and Rydberg states of these core-excited states, the electronic part of the

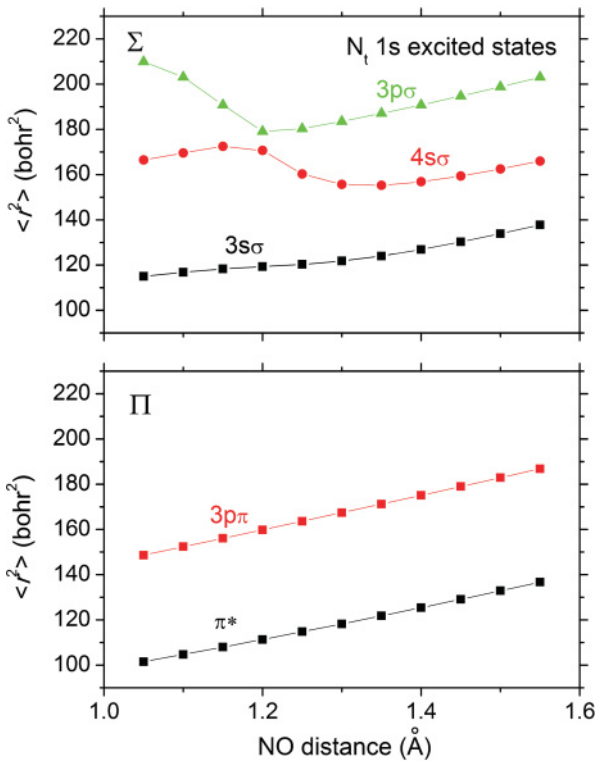

FIG. 7. (Color online) Second moments of the low-lying N_t 1*s* excited states of N_2O in Σ and Π symmetry with the cut at $R_{NN} = 1.10$ Å. Calculations were carried out using the SAC-CI ECM method.

second moment $\langle r^2 \rangle$ was calculated. The results of the N_t 1*s* excited states are shown in Fig. 7. As can be seen, the second moment of the N_t $1s^{-1}$ π^*, $3p\pi$, and $3s\sigma$ states increases as the NO distance is elongated. However, the second moment of the $4s\sigma$ state in the diabatic picture shows an irregular behavior; that is, the electronic distribution shrinks as the NO distance becomes larger. This indicates that the coupling of the valence and Rydberg states becomes strong along this coordinate, as was also seen for the O $1s^{-1}$ $4s\sigma$ state [23]. The calculated value of this state, however, was $\langle r^2 \rangle = 180-190$ bohrs^2 in the FC region. This indicates that the coupling of the valence and Rydberg states of the N_t $1s^{-1}$ $4s\sigma$ state is weak compared with the O $1s^{-1}$ $4s\sigma$ [23] and N_c $1s^{-1}$ $4s\sigma$ states, as discussed later.

The well-resolved line in the TIY spectrum at 406.99 eV is essentially the N_t $1s^{-1}$ $3d\pi$ Rydberg state [16,22], as seen from the ARIY [I(90°)] recording. As indicated in the ARIY [I(90°)] spectrum, there may also be a (100) vibrational component underneath the adjacent spectral feature, the (000) line of the N_t $1s^{-1}$ $4p\pi$ Rydberg state centered at 407.25 eV (p11). Furthermore, at least one additional vibrational component of the N_t $1s^{-1}$ $4p\pi$ Rydberg state, the (100) line, can be identified at 407.42 eV photon energy (p12) in the ARIY [I(90°)] spectrum. By looking again at the upper panel of Fig. 2, the latter line, however, cannot fully account for the comparatively high intensity in the TIY spectrum at this photon energy. In fact, by comparing the spectral profiles of the TIY, ARIY [I(0°)] and ARIY [I(90°)] recordings around 407.42 eV and above, we can see that particular states of Σ symmetry are rather prominent in this region. Our analysis of the quantum defects of suitable Rydberg states suggests assignments of the various spectral features as included in the middle and lower panels of Fig. 2, respectively, and as summarized in Table I. The presence of the N_t $1s^{-1}$ $np\pi$ series in this spectral region has been proposed by Prince *et al.* [22], and the assignment of the N_t $1s^{-1}$ $4s\sigma$ and $5s\sigma$ states has recently been tentatively proposed by Adachi *et al.* [16]. The appearance of Σ states at ~407.85 eV photon energy and higher, tentatively assigned here as higher N_t $1s^{-1}$ $ns\sigma$ Rydberg members, is perhaps not totally unexpected because the lower members of this series exhibit an extraordinarily high intensity, which is presumably caused by an underlying mixing of the valence and Rydberg states [16].

The corresponding SAC-CI PESs of the N_t $1s^{-1}$ $4p\sigma$, $5s\sigma$, $4p\pi$, and $5p\pi$ states are also displayed in Figs. 3 and 4. The calculated energy positions of the N_t $1s^{-1}$ $4p\pi$, $4p\sigma$, and $5s\sigma$ states are consistent with the present ARIY assignments shown in Fig. 2 and Table I, although a detailed vibrational analysis was not performed for these states. The vibrational structure of the N_t $1s^{-1}$ $4p\sigma$ and $5s\sigma$ states in the ARIY spectrum is similar to that of the N_t $1s^{-1}$ $3p\sigma$ and $4s\sigma$ states. In accordance with the ARIY spectra, the PESs of the N_t $1s^{-1}$ $4p\sigma$ and $5s\sigma$ states interact with each other in a similar way to those of the $3p\sigma$ and $4s\sigma$ states represented in Figs. 3 and 4.

B. N_c 1*s* excitation

Figure 8 shows the 409–413-eV photon energy region of the TIY photoabsorption spectrum of N_2O (upper panel) alongside the corresponding ARIY measurements [I(0°) middle panel; and I(90°) lower panel]. The N_c 1*s* ionization threshold, located

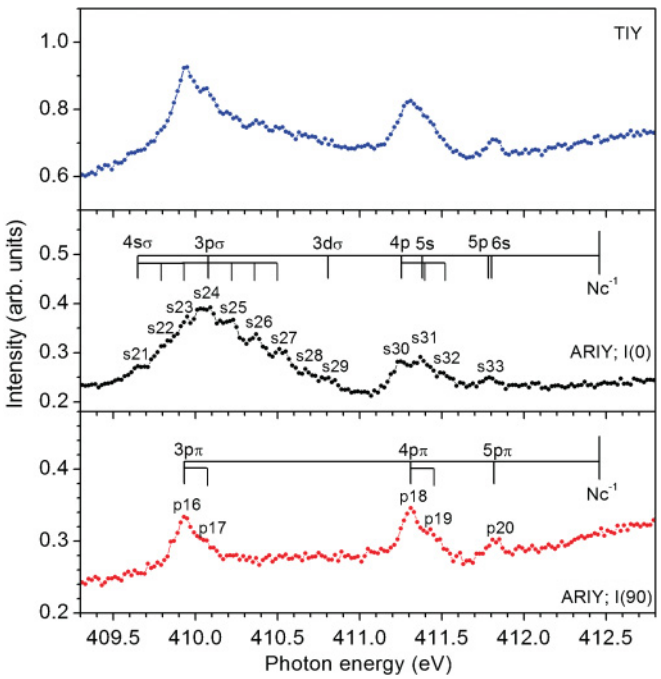

FIG. 8. (Color online) High-resolution oxygen *K*-edge total ion yield (TIY) and angle-resolved ion yield (ARIY) spectra of N_2O recorded in the photon energy range between 409 and 413 eV. Upper panel: TIY spectrum; middle panel: ARIY spectrum of the Σ channels ($\Delta\Lambda = 0$); lower panel: ARIY spectrum of the Π channels ($\Delta\Lambda = 1$).

TABLE III. Vertical excitation energy (ΔE) and oscillator strength (f) of the N 1s transitions calculated by the SAC-CI method at $R_{NN} = 1.127$ Å and $R_{NO} = 1.185$ Å.

State	ΔE (eV)	f
N_t 1s		
3$s\sigma$	405.4	0.0042
3$p\sigma$	407.6	0.0073
4$s\sigma$	408.1	0.0022
4$p\sigma$	408.8	0.0049
5$s\sigma$	409.0	0.0006
π^*	402.2	0.0500
3$p\pi$	407.4	0.0028
4$p\pi$	408.8	0.0008
5$p\pi$	409.3	0.0004
N_c 1s		
3$s\sigma$	409.4	0.0010
3$p\sigma$	412.1	0.0002
4$s\sigma$	411.8	0.0012
4$p\sigma$	413.0	0.0000
5$s\sigma$	413.2	0.0004
π^*	405.7	0.0623
3$p\pi$	411.6	0.0002
4$p\pi$	412.9	0.0002
5$p\pi$	413.5	0.0002

at 412.44 eV [41], is marked in this figure as a reference for the spectral assignments made. The assignments are summarized in Table IV together with the previous results of Adachi *et al.* [16] and Prince *et al.* [22].

The corresponding SAC-CI ECM results of the PESs of the N_c 1s excited states, where a one-dimensional cut was made at $R_{NN} = 1.10$ Å, and the electronic part of the second moment $\langle r^2 \rangle$ for these states are displayed in Figs. 9 and 10, respectively. As can be seen, the PES of the N_c $1s^{-1}$ 3$s\sigma$ state is repulsive along the NO distance, which differs from that of the N_t $1s^{-1}$ 3$s\sigma$ state. The oscillator strengths of the N_c 1s transitions are given in Table III. The oscillator strength of the N_c $1s^{-1}$ π^* transition is large, whereas those of other transitions are much smaller. This trend is different from the N_t 1s transitions, which has also been found in previous work [16].

The measured TIY spectrum essentially consists of three gross features located at ~409.95 eV, 411.31 eV, and 411.83 eV photon energy, respectively, all of which get substantial contributions from states of Σ and Π symmetry; compare ARIY [I(0°)] and ARIY [I(90°)] spectra. The identification of the spectral features in the ARIY [I(90°)] recording is fairly straightforward using the quantum defect as a guide, and we essentially identify the same electronic states as previously reported [16,22]. Clearly, some of the N_c $1s^{-1}$ $np\pi$ Rydberg states are broadened. This is most likely because of vibrations of the ($\nu_1$00) mode with an energetic spacing of ~130 meV, as marked in Fig. 8.

The theoretical vibrational spectrum of the N_c $1s^{-1}$ 3$p\pi$ state is compared with the corresponding experimental spectrum in Fig. 11. The calculated bond distances of the N_c $1s^{-1}$ 3$p\pi$ state are $R_{NN} = 1.119$ Å and $R_{NO} = 1.243$ Å, and the ν_1 mode is active for the N_c $1s^{-1}$ 3$p\pi$ excitation; the p16 and p17 peaks are assigned to the (000) and (100) levels,

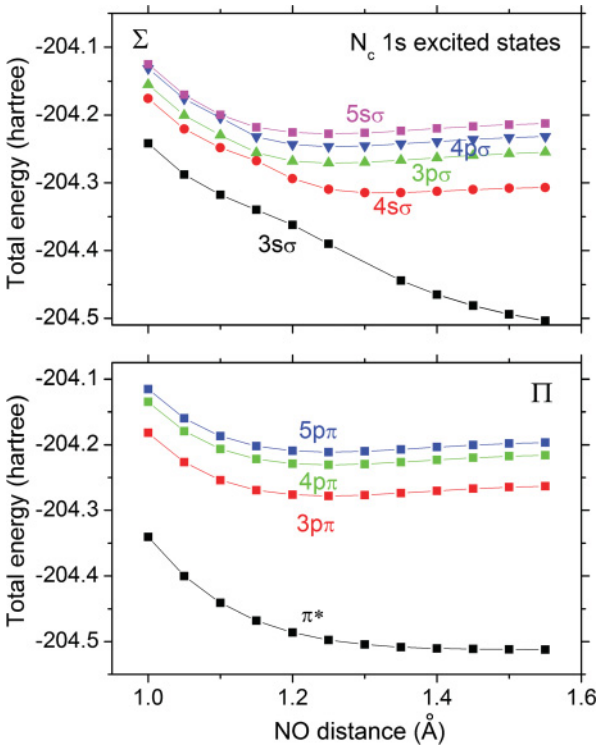

FIG. 9. (Color online) Potential energy curves of the low-lying N_c 1s excited states of N_2O in Σ and Π symmetry with the cut at $R_{NN} = 1.10$ Å. Calculations were carried out using the SAC-CI ECM method.

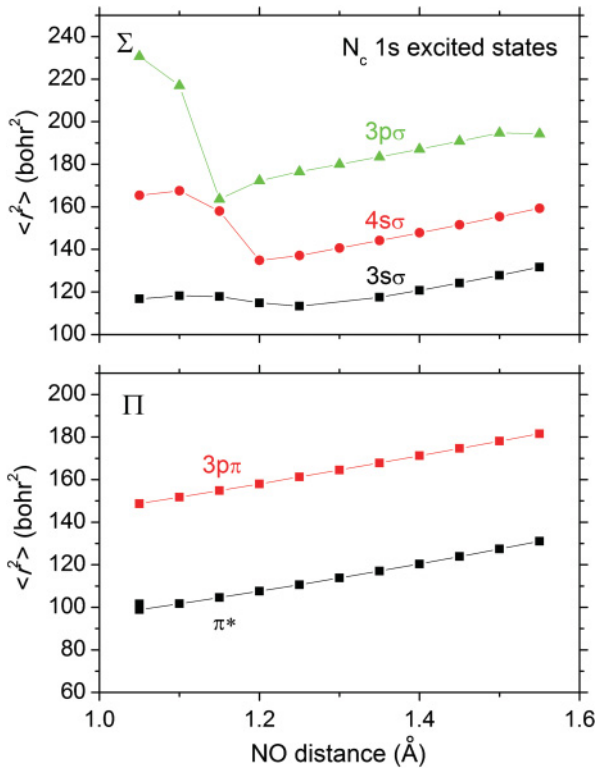

FIG. 10. (Color online) Second moments of the low-lying N_c 1s excited states of N_2O in Σ and Π symmetry with the cut at $R_{NN} = 1.10$ Å. Calculations were carried out using the SAC-CI ECM method.

TABLE IV. Energies, assignments and quantum defect δ for the N_c 1*s* Rydberg states identified in the angle-resolved ion yield spectrum of Fig. 8.

Peak	Expt. (eV)	Theory (eV)	Assignment	δ	Prince	Adachi
s21	409.65	409.65[a]	$4s\sigma$ (N_c)	0.80		
s22	409.81	409.78	$4s\sigma$ (N_c) (100)		$3p\sigma$ (N_c)	
p16	409.93	409.93[b]	$3p\pi$ (N_c)	0.68	$3p\pi$ (N_c)	$3p\pi$ (N_c)
s23	409.95	409.94	$4s\sigma$ (N_c) (200)			
p17	410.06	410.05	$3p\pi$ (N_c) (100)	0.68	$3p\pi$ (N_c) (001)	
s24	410.07	410.14[c]	$3p\sigma$ (N_c)	1.61		$3p\sigma$ (N_c)
		410.11	$4s\sigma$ (N_c) (300)			$3d\sigma$ (N_c)
s25	410.20	410.26	$3p\sigma$ (N_c) (100)			
		410.20	$4s\sigma$ (N_c)			
s26	410.37	410.39	$3p\sigma$ (N_c) (200)		$4s\sigma$ (N_c)	
		410.38	$4s\sigma$ (N_c)			
s27	410.51	410.51	$3p\sigma$ (N_c) (300)		$4s\sigma$ (N_c) + ν	
		410.45	$4s\sigma$ (N_c)			
s28	410.67	410.56	$4s\sigma$ (N_c)			
		410.63				
s29	410.81		$3d\sigma$ (N_c)	0.13		
s30	411.25		$4p\sigma$ (N_c)	0.64		
p18	411.31		$4p\pi$ (N_c)	0.56	$4p\pi$ (N_c)	
s31	411.37		$5s\sigma$ (N_c)	1.45	$5s\sigma$ (N_c)	
p19	411.44		$4p\pi$ (N_c) (100)			
s32	411.50		$5s\sigma$ (N_c) (100)			
s33	411.79		$6s\sigma$ (N_c)	1.45		
p20	411.83		$5p\pi$ (N_c)	0.40		

[a]The calculated (000) level of the N_c $1s^{-1}$ $4s\sigma$ state is set to 409.65 eV.
[b]The calculated (000) level of the N_c $1s^{-1}$ $3p\pi$ state is set to 409.93 eV.
[c]The position of the (000) level of the N_c $1s^{-1}$ $3p\sigma$ state is calculated relative to the N_c $1s^{-1}$ $3p\pi$ state.

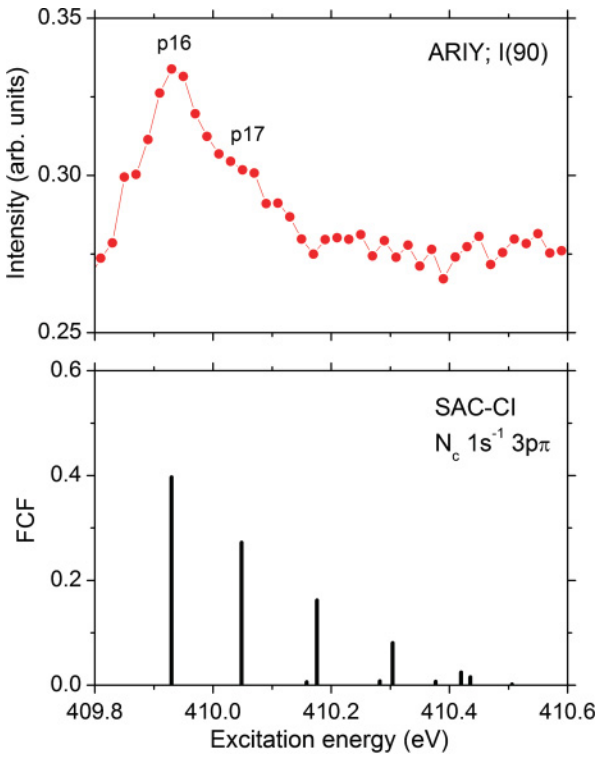

FIG. 11. (Color online) The ARIY [I(90°)] and SAC-CI ECM spectra of the N_c $1s^{-1}$ $3p\pi$ states of N_2O.

respectively. The energy separation was 120 meV, which compares well with the experimental value of 130 meV. The calculated FC factors show that the geometry change appears to be overestimated in the present calculations; higher ($\nu_1$00) levels are also populated.

The assignment of the peak structures in the ARIY [I(0°)] recording is more ambiguous, in particular because the first band at ~409.95 eV appears quite broad, as was pointed out in the study by Adachi *et al.* [16]. Large parts of the recording can certainly be attributed to the N_c $1s^{-1}$ $3p\sigma$ Rydberg state, and the superimposed fine structure, with a spacing of ~160 meV, suggests excitation of vibrations of the ($\nu_1$00) mode. However, none of the other Rydberg states we observed had such an extended progression, and because the PESs of the excited Rydberg states are usually nearly equal to that of the ionized states, this finding is surprising. Whether or not the N_c $1s^{-1}$ $3d\sigma$ and/or the N_c $1s^{-1}$ $4s\sigma$ Rydberg states, as marked in the figure, contribute to the intensity of this band is difficult to judge, in particular because their excitations are expected to be rather weak due to symmetry reasons [16]. An underlying mixing of the valence and Rydberg states, as proposed by Adachi *et al.* [16] for other states, could give rise to such an extended vibrational progression, akin to the O 1*s* $4s\sigma$ Rydberg state in N_2O (e.g. [10] and references therein).

In the theoretical results of this energy region, the relative energies of the N_c $1s^{-1}$ $3p\sigma$ and $4s\sigma$ states in the FC region are delicate; the N_c $1s^{-1}$ $4s\sigma$ state is stable compared with the N_c $1s^{-1}$ $3p\sigma$ state. The calculated vibrational spectra of these

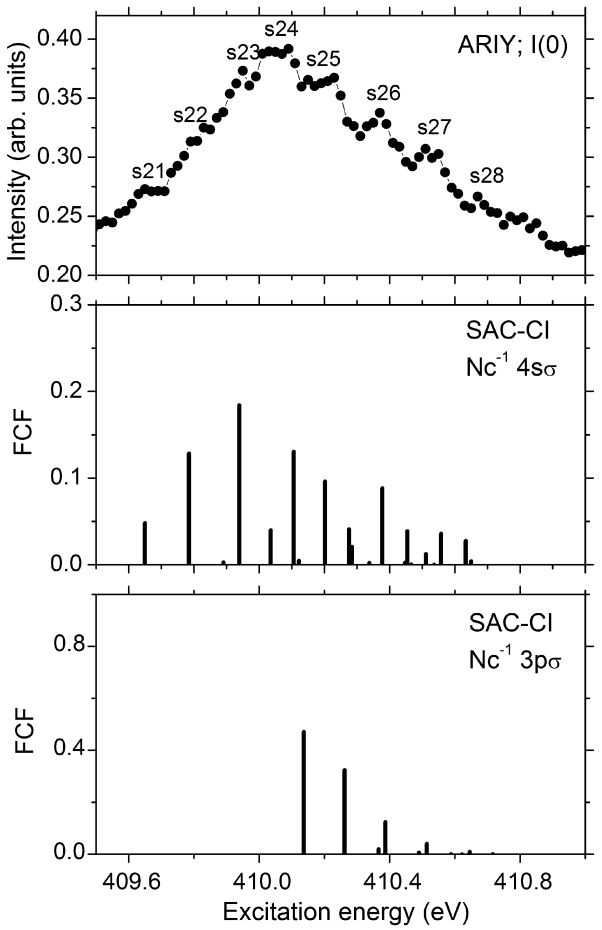

FIG. 12. The ARIY [I(0°)] and SAC-CI ECM spectra of the N_c $1s^{-1}$ $4s\sigma$ and N_c $1s^{-1}$ $3p\sigma$ states of N_2O.

states are compared with the experimental spectrum in Fig. 12. The excitation energy of the N_c $1s^{-1}$ $3p\sigma$ state was calculated relative to the N_c $1s^{-1}$ $3p\pi$ state, whereas the excitation energy of the N_c $1s^{-1}$ $4s\sigma$ state was shifted by +0.8 eV to fit the calculated (000) peak to the s21 peak in the ARIY spectrum using the SAC-CI ECM results. As can be seen in the calculated N_c $1s^{-1}$ $4s\sigma$ spectrum, the higher vibrational levels of the N_c $1s^{-1}$ $4s\sigma$ state were excited, which can be understood from the large geometry change of this state; $R_{NN} = 1.112$ Å and $R_{NO} = 1.314$ Å, which was also found for the O $1s^{-1}$ $4s\sigma$ state [23]. From the calculated ionization energy relative to the N_c $1s^{-1}$ $3p\pi$ state, the vibrational spectrum of the N_c $1s^{-1}$ $3p\sigma$ state seems to start around the s24 peak. The calculated equilibrium bond distances of the N_c $1s^{-1}$ $3p\sigma$ state were $R_{NN} = 1.127$ Å and $R_{NO} = 1.243$ Å, which are similar to those of the N_c $1s^{-1}$ $3p\pi$ state. The oscillator strengths of the N_c $1s^{-1}$ $3p\sigma$ and $4s\sigma$ transitions at the ground-state geometry are $f = 0.0002$ and 0.0012, respectively, and, therefore, the observed band can predominantly be attributed to the N_c $1s^{-1}$ $4s\sigma$ transition. This also explains the irregular behavior of the vibrational progression of this band due to the N_c $1s^{-1}$ $4s\sigma$ transition. The second moment of the N_c $1s^{-1}$ $4s\sigma$ state in the FC region is $\langle r^2 \rangle = 140-160$ bohrs^2 and the electronic distribution shrinks. Therefore, the coupling of the valence and Rydberg states of the N_c $1s^{-1}$ $4s\sigma$ state is relatively strong as in the O $1s^{-1}$ $4s\sigma$ state [23].

The remaining spectral features in the ARIY [I(0°)] spectrum, located at 411.23 eV (p18) and 411.79 eV (p20) photon energy, have been revealed for the first time in this study, and can be assigned to the N_c $1s^{-1}$ $4p\sigma$ and N_c $1s^{-1}$ $5p\sigma$ Rydberg states, respectively, based on evaluation of the quantum defect. The comparatively broad band at 411.23 eV also reflects some fine structure of ~160 meV spacing, suggesting ($\nu_1$00) vibrations of the N_c $1s^{-1}$ $4p\sigma$ Rydberg state. Some contribution from the N_c $1s^{-1}$ $5s\sigma$ Rydberg states may also play a role; however, they are expected to be rather weak due to symmetry reasons [16]. Finally, the PESs of the N_c $1s^{-1}$ $4p\sigma$, $5s\sigma$, $4p\pi$, and $5p\pi$ states were also computed as shown in Fig. 9. The relative energy positions of the N_c $1s^{-1}$ $4p\sigma$ and $5s\sigma$ states are consistent with the present experimental assignment.

V. SUMMARY

We have investigated vibrational fine structure in the N_t $1s$ and N_c $1s$ absorption spectra of N_2O using high-resolution ARIY spectroscopy and accurate SAC-CI and SAC-CI ECM calculations. The equilibrium structures and the 2D PESs of the N_t $1s$ and N_c $1s$ excited states with respect to $3p\pi$, $3p\sigma$, and $4s\sigma$ transitions were calculated to analyze in detail the spectral features observed and reveal geometry changes in the electronic states studied. The theoretical spectrum reproduced the experimental observations well, which were specific to individual Rydberg states and gave quantitative assignments of the vibrational fine structure in these states. The coupling of the valence and Rydberg states of these states was examined based on second moment analysis. Irregular Rydberg behavior was found in the N_c $1s^{-1}$ $4s\sigma$ state.

ACKNOWLEDGMENTS

This study was carried out with the approval of the SPring-8 Program Review Committee. This study was supported by JST-CREST, a Grant-in-Aid for Scientific Research from the Japanese Society for the Promotion of Science (JSPS) and the Next Generation Supercomputing Project. R.F. acknowledges financial support from the Swedish Research Council (V.R.) and would like to thank Tohoku University for their hospitality and financial support. The computations were partly performed at the Research Center for Computational Science in Okazaki, Japan.

[1] J. Stöhr, *NEXAFS Spectroscopy* (Springer, Berlin, 1992).
[2] I. Nenner and P. Morin, in *VUV and Soft X-ray Photoionization*, edited by U. Becker and D. A. Shirley (Plenum, New York, 1996).
[3] A. P. Hitchcock, Phys. Scr., T **31**, 159 (1990).
[4] M. Nakamura *et al.*, Phys. Rev. **178**, 80 (1969).
[5] N. Saito and I. H. Suzuki, Phys. Rev. Lett. **61**, 2740 (1988).

[6] A. Yagishita, H. Maezawa, M. Ukai, and E. Shigemasa, Phys. Rev. Lett. **62**, 36 (1989).
[7] K. Lee, D. Y. Kim, C. I. Ma, D. A. Lapiano-Smith, and D. M. Hanson, J. Chem. Phys. **93**, 7936 (1990).
[8] R. N. Zare, Mol. Photochem. **4**, 1 (1972).
[9] G. E. Busch and K. R. Wilson, J. Chem. Phys. **56**, 3638 (1972).
[10] J. Adachi, N. Kosugi, and A. Yagishita, J. Phys. B: At. Mol. Opt. Phys. **38**, R127 (2005).
[11] J. Murakami, M. C. Nelson, S. L. Anderson, and D. M. Hanson, J. Chem. Phys. **85**, 5755 (1986).
[12] G. R. Wight and C. E. Brion, J. Electron Spectrosc. Relat. Phenom. **3**, 191 (1974).
[13] M. Tronc, G. C. King, and F. H. Read, J. Phys. B: At. Mol. Phys. **13**, 999 (1980).
[14] A. Bianconi, H. Petersen, F. C. Brown, and R. Z. Bachrach, Phys. Rev. A **17**, 1907 (1978).
[15] Y. Ma, C. T. Chen, G. Meigs, K. Randall, and F. Sette, Phys. Rev. A **44**, 1848 (1991).
[16] J. Adachi, N. Kosugi, E. Shigemasa, and A. Yagishita, J. Chem. Phys. **102**, 7369 (1995).
[17] T. LeBrun, M. Lavoll, M. Simon, and P. Morin, J. Chem. Phys. **98**, 2534 (1993).
[18] J. D. Bozek, N. Saito, and I. H. Suzuki, J. Chem. Phys. **98**, 4652 (1993).
[19] J. Adachi, N. Kosugi, E. Shigemasa, A. Yagishita, and P. A. Hatherly, J. Electron Spectrosc. Relat. Phenom. **79**, 491 (1996).
[20] M. Machida, M. Lavoll, J. Randrianjafisoa, G. Laurent, M. Nagoshi, K. Okada, I. Koyano, and N. Saito, J. Chem. Phys. **120**, 3635 (2004).
[21] T. Tanaka *et al.*, Chem. Phys. Lett. **428**, 34 (2006).
[22] K. C. Prince, L. Avaldi, M. Coreno, R. Camilloni, and M. de Simone, J. Phys. B: At. Mol. Opt. Phys. **32**, 2551 (1999).
[23] T. Tanaka *et al.*, Chem. Phys. Lett. **435**, 182 (2007).
[24] T. Tanaka *et al.*, Phys. Rev. A **77**, 012709 (2008).
[25] H. Nakatsuji, Chem. Phys. Lett. **59**, 362 (1978).
[26] H. Nakatsuji, Chem. Phys. Lett. **67**, 329 (1979).
[27] M. Ehara, J. Hasegawa, and H. Nakatsuji, *SAC-CI Method Applied to Molecular Spectroscopy, in Theory and Applications of Computational Chemistry: The First 40 Years, A Volume of Technical and Historical Perspectives* (Elsevier, Amsterdam, 2005).
[28] M. Ehara *et al.*, J. Chem. Phys. **124**, 124311 (2006).
[29] M. Ehara *et al.*, J. Chem. Phys. **125**, 114304 (2006).
[30] H. Ohashi, E. Ishiguro, Y. Tamenori, H. Kishimoto, M. Tanaka, M. Irie, T. Tanaka, and T. Ishikawa, Nucl. Instrum. Methods A **467–468**, 529 (2001).
[31] H. Ohashi *et al.*, Nucl. Instrum. Methods A **467–468**, 533 (2001).
[32] T. Tanaka and H. Kitamura, Nucl. Instrum. Methods A **364**, 368 (1995).
[33] T. Tanaka and H. Kitamura, J. Synchrotron Radiat. **3**, 47 (1996).
[34] N. Saito *et al.*, Phys. Rev. A **62**, 042503 (2000).
[35] T. H. Dunning Jr., J. Chem. Phys. **90**, 1007 (1989).
[36] K. Kaufmann, C. Nager, and M. Jungen, Chem. Phys. **95**, 385 (1985).
[37] J. L. Teffo and A. Chedin, J. Mol. Spectrosc. **135**, 389 (1989).
[38] R. Fukuda and H. Nakatsuji, J. Chem. Phys. **128**, 094105 (2008).
[39] M. J. Frisch *et al.*, GAUSSIAN09, Rev. B.01, Gaussian, Inc., Wallingford, CT, 2010.
[40] G. A. Worth, M. H. Beck, A. Jackle, and H.-D. Meyer, The MCTDH Package, Version 8.3, Heidelberg University, Heidelberg, Germany, 2003.
[41] M. Alagia *et al.*, Phys. Rev. A **71**, 012506 (2005).
[42] O. Edqvist, E. Lindholm, L. E. Selin, L. Åsbrink, C. E. Kuyatt, S. R. Mielczarek, J. A. Simpson, and I. Fischer-Hjalmars, Phys. Scr. **1**, 172 (1970).
[43] G. Herzberg, *Infrared and Raman Spectra* (D. Van Nostrand, New York, 1951).